Wiley
International Journal of Energy Research
Volume 2024, Article ID 1119181, 16 pages
https://doi.org/10.1155/2024/1119181

WILEY

Research Article

Improved Monitoring of Wind Speed Using 3D Printing and Data-Driven Deep Learning Model for Wind Power Systems

Sanghun Shin,[1] **Sangyeun Park**,[1] **and Hongyun So**[1,2]

[1]*Department of Mechanical Engineering, Hanyang University, Seoul 04763, Republic of Korea*
[2]*Institute of Nano Science and Technology, Hanyang University, Seoul 04763, Republic of Korea*

Correspondence should be addressed to Hongyun So; hyso@hanyang.ac.kr

Received 25 February 2024; Revised 10 July 2024; Accepted 3 August 2024

Academic Editor: Abdulkerim Okbaz

This study presents a novel method for airflow rate (i.e., wind speed) sensing using a three-dimensional (3D) printing-assisted flow sensor and a deep neural network (DNN). The 3D printing of thermoplastic polyurethane can realize multisensing devices for different flow rate values. Herein, the 3D-printed flow sensor with an actuating membrane is used to simultaneously measure two electrical parameters (i.e., capacitance and resistance) depending on the airflow rate. Subsequently, a data-driven DNN model is introduced and trained using 6,965 experimental data points, including input (resistance and capacitance) and output (airflow rate) data with and without external interferences during capacitance measurements. The mean absolute error (MAE), mean squared error (MSE), and root mean squared logarithmic error (RMSLE) measured using predicted flow rate values by the DNN model with multiple inputs are 0.59, 0.7, and 0.18 for continuous test dataset without interference and 1.16, 3.95, and 0.73 for test dataset with interference, respectively. Compared to the prediction results using single-input cases, the average MAE, MSE, and RMSLE significantly decrease by 70.37%, 88.74%, and 72.26% for test datasets without interference and 51.91%, 53.01%, and 12.20% with interference, respectively. The results suggest a cost-effective and accurate sensing technology for wind speed monitoring in wind power systems.

1. Introduction

The amount of electricity generated by a wind power system highly depends on the local wind speed. In general, the wind speed relies on several factors such as location of a wind turbine, obstructions (trees or buildings nearby), and installation height. Because the electricity generated by a wind turbine is generally proportional to the wind speed [1, 2], it is important to precisely measure the wind speed (or flow rate) potential before installing a wind power system to make sure it will be financially worthwhile [3]. For facile fabrication of flow monitoring sensors, three-dimensional (3D) printing, also known as additive manufacturing, has been extensively studied and employed in various fields in the past few decades owing to its versatile, simple, and cost-effective fabrication methods. Therefore, various printing strategies, such as stereolithography [4, 5], fused deposition modeling (FDM) [6, 7, 8], selective laser sintering [9, 10], and digital light process [11, 12], have been developed to meet the increasing demand. Compared to traditional fabrication processes, 3D printing-based methods have been considered future manufacturing technologies owing to the direct printing of microscale patterns and atypical morphology, which allows customized production without additional equipment. Direct 3D printing methods have been adopted for manufacturing functional devices, such as sensors [8, 13, 14], microfluidic chips [6, 15, 16], and actuators [17, 18, 19], using printable material with different mechanical properties (e.g., elastic modulus, thermal conductivity, and electrical conductivity). Thermoplastic polyurethane (TPU) filaments have been widely used for flexible structures because of their biocompatibility [20, 21] and rubber-like characteristics without additional chemical cross-linking [22]. Consequently, 3D soft material printing technology can offer innovative and novel fabrication processes for complex morphologies for future applications, such as soft robotics, grippers, actuators, and sensors.

Flexible polymer-based functional devices find applications in strain and pressure sensors. In addition, unlike conventional rigid sensors, soft devices exhibit deformable characteristics that depend on the target. Thus, by combining

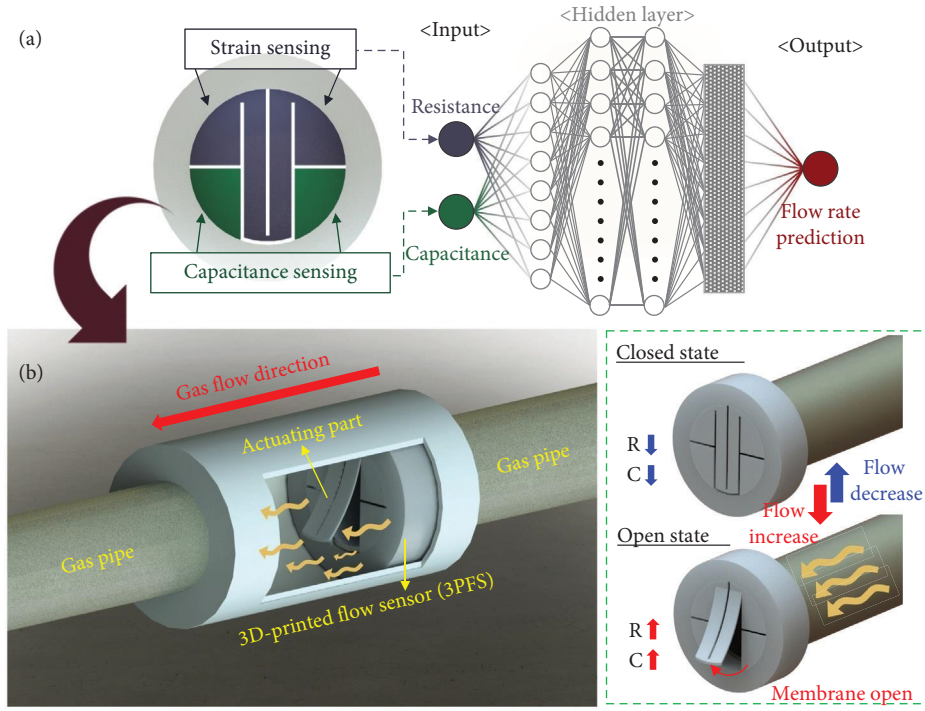

FIGURE 1: Schematic of (a) flow rate sensing systems, including a 3D-printed device and deep neural network algorithm for sensor fusion, and (b) sensing principle of the 3PFS for airflow rate measurement.

FDM or direct ink writing methods, efforts to expand the soft device applications are being made [8, 23]. However, soft material-based devices have two fundamental drawbacks: nonlinearity and hysteresis [24, 25, 26]. Therefore, further theoretical and experimental approaches are required to obtain reliable results.

With the development of artificial intelligence, deep learning-based data-driven models are being considered for complicated nonlinear problems [24, 27]. Deep learning models have recently gained remarkable success in numerous applications, such as natural language processing [28, 29], computer vision [30, 31], and regression analysis [32, 33]. Notably, deep neural networks (DNNs) with multilayer architectures have been widely applied for regression analysis of experimental data [33, 34]. The data-driven model suggests nonlinear relationships between the input and output data through multiple nonlinear transformations of the stacked layers. In addition, there have been numerous efforts to enhance the accuracy of deep learning models; these efforts include selecting an effective architecture [24, 35, 36], multiple sensor data fusion [36, 37], and hyperparameter tuning [33, 38]. Thus, deep learning regression models can play a pivotal role by integrating with soft material devices via appropriate supervised learning techniques in real applications.

Among various functional devices, flow rate sensors are essential in diverse industries for environmental monitoring. The flow sensors can be categorized into thermal and nonthermal types [39, 40]. Among them, thermal-type flow sensors evaluate changes in heat distribution affected by the mass flow rate using heating elements, thus offering the advantages of high accuracy and sensitivity. In contrast, nonthermal-type flow sensors use mechanical/electrical signals (e.g., change in pressure [41, 42], resistance [43, 44], and capacitance [45, 46, 47]) without additional power-consuming heaters for measurement via manipulated structures [41, 42] or moving components, such as cantilevers [43, 44] and paddles [45]. Traditionally, the flow sensors have been implemented using microelectromechanical system (MEMS)-based processes [39, 40, 45, 46]. However, such conventional methods necessitate intricate fabrication steps, a clean room environment, and hazardous chemical treatments, leading to high production costs. Therefore, the development of low-cost and accurate flow sensing systems through a simplified manufacturing process is highly required.

To date, various efforts to monitor the fluid flow have been conducted employing novel fabrication methods and deep learning approaches. For example, Daniel et al. [48] demonstrated a hot wire anemometer using a complete 3D printing method, while further optimization was required. In addition, Wang et al. [49] utilized machine learning models including the DNN algorithm to predict the oil/gas/water three-phase flow rate by combining various sensing parameters. Furthermore, Manami et al. [50] also utilized deep learning models to measure the two-phase flow rate with a measured dataset comprising 4,112 experimental samples.

In this study, a combination of a 3D-printed flow sensor (3PFS) with a deep learning model was implemented for airflow rate monitoring. The overall principle of the proposed method is illustrated in Figure 1. The fabricated 3PFS containing strain (blue area) and capacitance (green area) sensing areas is shown in Figure 1(a). As the actuating part in the middle moves due to the change in flow rate, the changed resistance and capacitance are obtained simultaneously. The

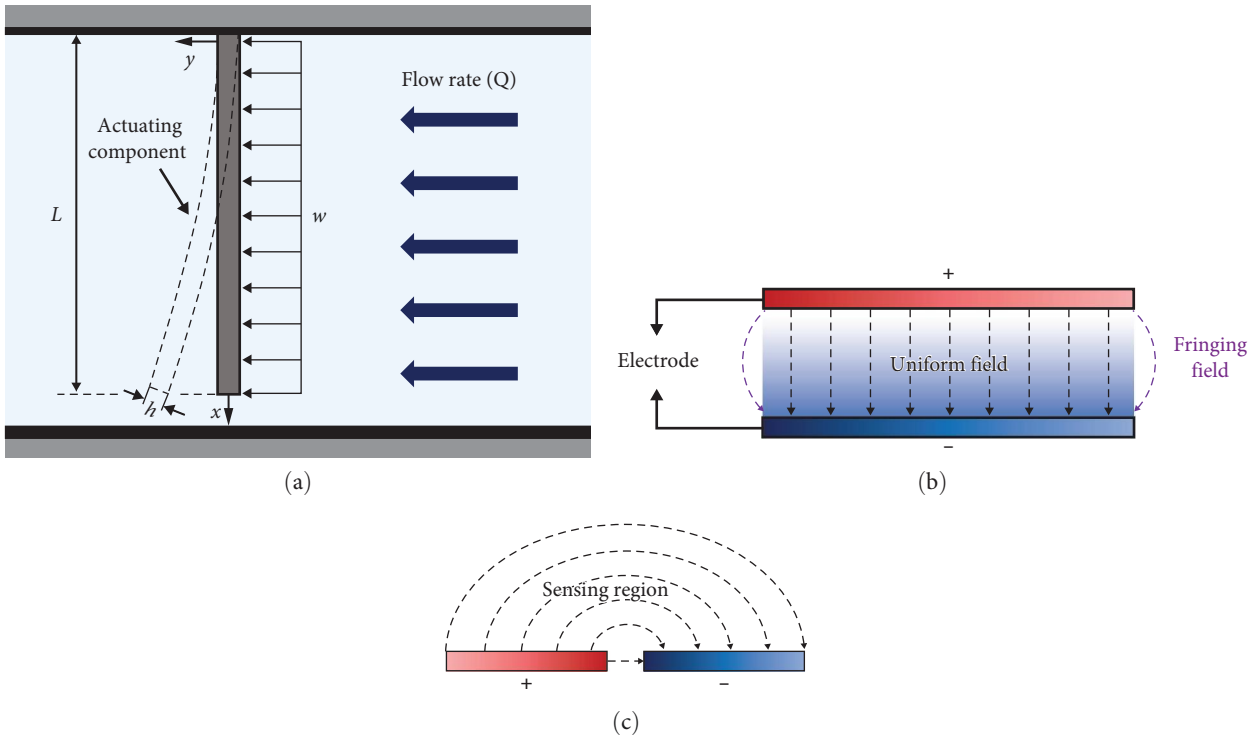

FIGURE 2: (a) Schematic of actuating membrane deflection for the nonthermal flow sensing. Illustrations of different capacitor types: (b) parallel-type capacitor and (c) coplanar-type capacitor.

3PFS can be adapted to the shape or size of any gas pipe by changing the 3D printing design, as shown in Figure 1(b). As the airflow bends the actuating part, the resistance increases owing to the generated cracks on the conductive layer (i.e., strain sensor). Simultaneously, as the actuating part that interferes with the electric field of the electrodes moves away, the coplanar capacitance increases. Finally, the flow rate is predicted using a DNN regression model, which is trained with the experimentally acquired dataset, and the prediction performance is compared under different input conditions. In addition, the transient sensing performance with and without external interference from adjacent objects is compared to confirm robust prediction. Consequently, this study aims to develop cost-effective flow sensor fabrication, which can measure different types of signals, and DNN-based sensor fusion technology to enhance prediction accuracy. The findings support a novel fabrication and analysis method that combines 3D printing and artificial intelligence for diverse gas-flow sensing applications.

2. Sensing Principle

For 3PFS, a polymer membrane fixed to a flow channel actuated by an external fluid flow was used for the nonthermal-type flow rate sensing methods. As illustrated in Figure 2(a), the flexible membrane with length L (m) deflects when the element is exposed to a uniformly distributed load w (N/m) by the drag force (normal force, F_D) which can be expressed as follows:

$$F_D = \frac{1}{2} C_D \rho S_p U^2, \tag{1}$$

where C_D, ρ, S_p, and U are drag force coefficient (dimensionless), air density, area of the membrane which is perpendicular to the flow, and airflow velocity, respectively. In this case, if the actuating membrane is assumed to be an elastic beam, the deflection tendency within the flow channel can be explained by applying a theoretical approximation using a simplified cantilever model [51, 52]. Thus, for the finite loads, differential equation of the deflection can be expressed as

$$\frac{d^2y}{dx^2} = \frac{M}{EI}, \tag{2}$$

where y, M, E, and I stand for deflection at x, bending moment, elastic modulus, and area moment of inertia, respectively. From Equation (2), the maximum deflection of a membrane with a given length (L) and distributed load (w) (Figure 2(a)) can be derived as follows [51]:

$$y_{max} = \frac{wL^4}{8EI} = \frac{F_D L^3}{8EI}. \tag{3}$$

When deformation of a substrate occurs due to bending or tensile forces, crack-based strain gauge was employed for the detection. Depending on the sensitivity of the strain gauge, resistance change (ΔR) by the strain can be calculated as follows [53, 54]:

$$\frac{\Delta R}{R_0} = \mathrm{GF} \times \varepsilon_s, \tag{4}$$

where R_0, GF, and, ε_s are initial resistance, gauge factor, and mechanical strain of the strain gauge. To calculate the generated strain of the strain sensor on the stretching surface of the bending membrane, the simplified cantilever model, assuming the rectangular cross section of b and h for width and thickness, can be utilized for the approximation as follows [55]:

$$\sigma(x) = \frac{M(x)}{I} \times \left(\frac{h}{2}\right), \tag{5}$$

$$M(x) = \frac{F_D(L-x)^2}{2L}, \tag{6}$$

where $\sigma(x)$ and $M(x)$ are bending stress and moment at x, respectively. In addition, the area moment of inertia (I) is given by $bh^3/12$ for the rectangular cross section. By integrating Equations (1), (5), and (6), the average strain detected by the strain sensor (ε_s) where the gauge length is L_s can be derived as follows:

$$\varepsilon(x) = \frac{\sigma(x)}{E} = \frac{C_D \rho S_p h}{8EIL}(L-x)^2 U^2, \tag{7}$$

$$\varepsilon_s = \frac{1}{L_s}\int_0^{L_s} \varepsilon(x)dx. \tag{8}$$

Therefore, the resistance change of the conductive layer on the bent membrane in response to the external fluid flow can be estimated as a function of fluid velocity U according to Equations (4) and (8).

In addition, among the various conventional nondestructive evaluation (NDE) methods, the coplanar capacitive sensing method has been considered one of the effective techniques with diverse advantages, including rapid response, nonradiative, and noninvasive characteristics [56]. Figures 2(b) and 2(c) illustrate basic structures of the parallel plate and coplanar capacitance. In the case of parallel capacitance, most of the electric field is generated uniformly between the two electrodes. On the other hand, a nonuniform fringing field, which can be utilized for NDE, is also generated at the edges, as shown in Figure 2(b). However, as the parallel type requires double-sided access to the target and the strong electric field region, it is not suitable for NDE in practical applications.

As shown in Figure 2(c), coplanar-oriented capacitive sensing approach can be utilized for NDE. The coplanar capacitors allow the fringing effect to dominate electric field formation, providing a larger probing area and single-sided access. When an object influencing the formation of an electric field in the sensing region exists, NDE can be performed through the variation of capacitance values. Therefore, the coplanar capacitive sensing method can be applied to proximity sensors [57] by detecting changes in permittivity.

According to the previous research, an analytical model for coplanar capacitive sensing can be established by using conformal mapping methods through an inverse-cosine transform [58]. Considering an electrode pair of a given

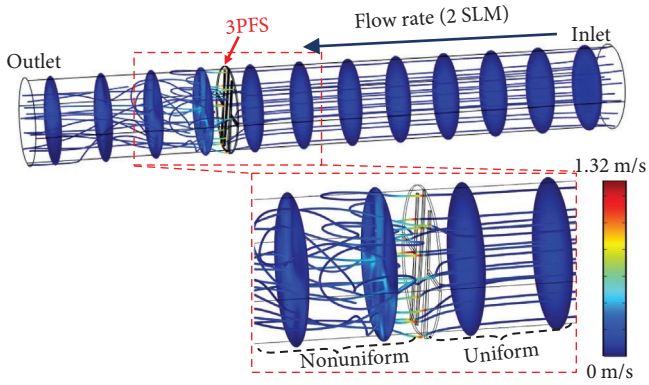

FIGURE 3: Simulation results of the velocity and streamline changed by the 3PFS.

width (w_e), gap ($2a$), and length (l), the capacitance (C) can be evaluated using the following equation [58, 59], provided that $l \gg w_e$ and $w_e/a \gg 1$.

$$C = \frac{2\varepsilon_r \varepsilon_0 l}{\pi} \ln\left[\left(1+\frac{w_e}{a}\right) + \sqrt{\left(1+\frac{w_e}{a}\right)^2 - 1}\right], \tag{9}$$

where ε_r and ε_0 are relative and vacuum permittivity, respectively. Furthermore, the capacitance can be also expressed considering the practical conditions according to the previous works as follows [57, 60]:

$$C = \eta \cdot \varepsilon_r \cdot l \cdot \left(\frac{w_e}{2a}\right)^{\frac{2}{\pi}\arctan\left(\frac{2a}{l}\right)} \cdot X^{\beta} \cdot Y^{\gamma}, \tag{10}$$

where X and Y are scale-independent values and η, β, and γ can be obtained through the experimental results. Thus, the capacitance values of the fixed coplanar electrodes changed by the different locations of adjacent objects in the sensing region. Consequently, strain and capacitance can be measured simultaneously through a membrane that bends in response to the external fluid flows by applying appropriate electrode arrangements, as seen in Figure 1.

Furthermore, to investigate the velocity and streamline changes during the fluid flow before and after passing through the 3PFS, a computational simulation was performed by using COMSOL Multiphysics® software with the fluid-structure interaction module. For the inlet boundary condition, 2 standard liters per minute (SLM), which corresponds to ~0.092 m/s, was applied to the inlet boundary condition. As shown in Figure 3, while the velocity may locally increase as it passes through internal structures, it should be noted that in incompressible flow, the flow rate passing through remains constant due to the continuity equation. Lastly, as the nonuniform streamline after passing through the 3PFS, an additional flow conditioner should be employed to correct the changed flow profile for a reliable flow field at the outlet for future applications.

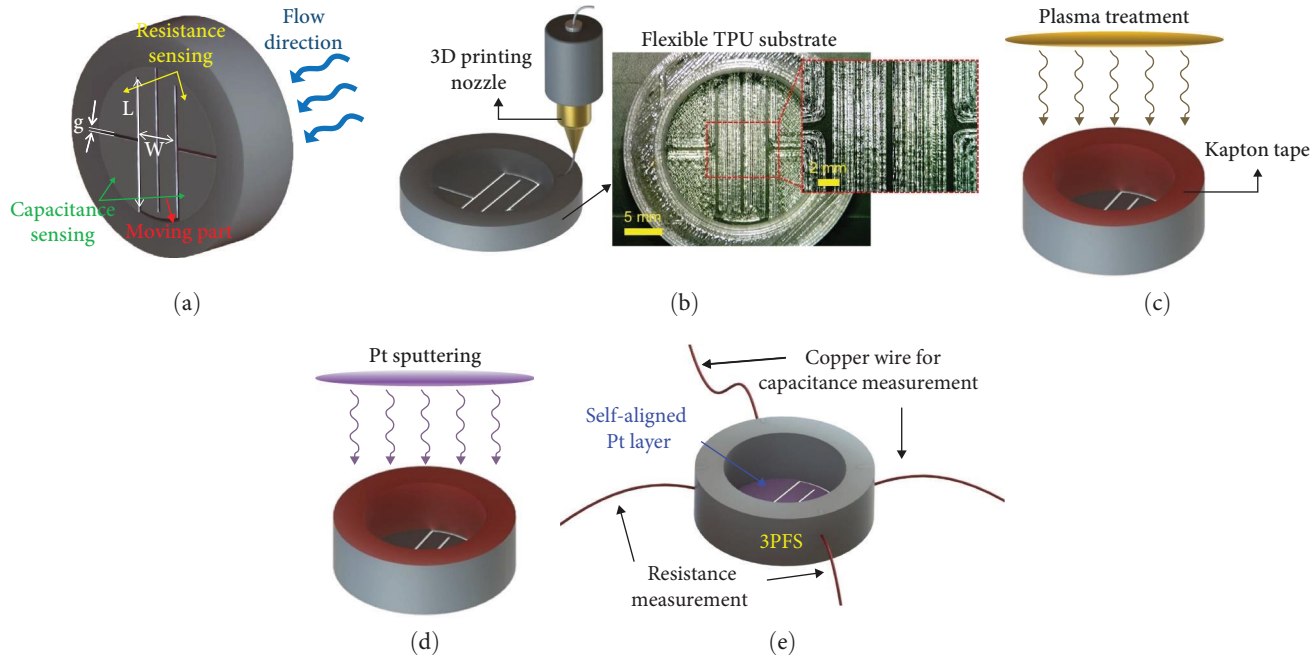

FIGURE 4: Overall fabrication process of the 3D-printed flow sensor. (a) Design parameters for capacitance/resistance sensing and moving membrane parts of 3PFS. (b) Direct TPU printing process for the body and main parts. (c) Plasma treatment onto the exposed active area for preprocessing before Pt deposition. (d) Pt sputtering onto the main body to produce a conductive layer. (e) Electrical connections for capacitance and resistance sensing.

3. Fabrication

Figure 4(a) illustrates the representative design parameters of the 3PFS. The gap between the patterns (g), length (L), and width (W) of the moving TPU membrane part were selected as 0.5, 19.13, and 6.5 mm. The sensor body has outer diameter, inner diameter, and height of 31.5 mm, 21.5 mm, and 10 mm, respectively, and the membranes for actuation and electrodes were 0.3-mm thick. Therefore, the flexible TPU membrane can freely move in response to the fluid flow. In addition, the changes in resistance due to strain on the surface and the simultaneous variations in coplanar capacitance resulting from the membrane movement can be measured separately. The geometrical parameters of the TPU substrate (i.e., membrane thickness and electrode area) were selected and designed considering the ease of 3D printing and inlet pressure change by comparing with the commercial orifice structures [61, 62] (Figures S1 and S2).

The 3PFS fabrication comprises four main steps: 3D printing of the TPU substrate, plasma treatment, metal sputtering for electrodes, and electrical connection with copper (Cu) wires. Figure 4(b) shows the printing process of the sensor substrate containing the main (i.e., membrane for actuation and electrodes) and body parts (i.e., flow channel for connection). The two-layer printing of the main part showed stable printing results. It should be noted that the size or shape of 3PFS can be easily modified by the additive manufacturing. Herein, an FDM-type 3D printer (Guider IIs, Zhejiang Flashforge 3D Technology Co., Ltd.) with a flexible TPU filament was used for printing. The printing conditions included filling density, printing speed, nozzle temperature, bed temperature, and layer thickness of 100%, 20 mm/s, 230°C, 60°C, and 0.15 mm, respectively. Subsequently, the main part was exposed before metal deposition by attaching Kapton tape onto the sensor body, as shown in Figure 4(c). No additional complex masking process is required because the required shape and patterns are formed during the printing process. Subsequently, oxygen plasma treatment for 30 s was performed for better adhesion, followed by a Pt sputtering process with a thickness of 20 nm, as depicted in Figure 4(d). Thus, separate strain and capacitance sensing parts were naturally formed by the 0.5 mm gap between the electrodes, thus allowing independent data collection. Finally, Cu wires were used to provide external electrical access to the self-aligned Pt electrode layer, as shown in Figure 4(e). The fabricated 3PFS via 3D printing and sputtering, replacing the traditional MEMS processes and complicated masking processes or lithography, demonstrates a facile and rapid fabrication method.

To characterize the thermal history of TPU filament and 3D-printed TPU, differential scanning calorimetry (DSC) measurements were conducted using a differential scanning calorimeter (DSC Q20, TA Instruments). The thermal cycle of heating–cooling process was performed for each sample with a heating and cooling rate of 20°C/min from −50 to 250°C under a nitrogen atmosphere. During the first thermal cycle, the glass transition (T_g), melting (T_m), and crystallization peaks (T_c) were obtained from the DSC thermograms of the two TPU samples, as seen in Figure 5. Notably, two distinct T_g values were identified for each sample, corresponding to soft and hard segments of the TPU [63, 64]. The T_g values for the soft and hard segments of the TPU

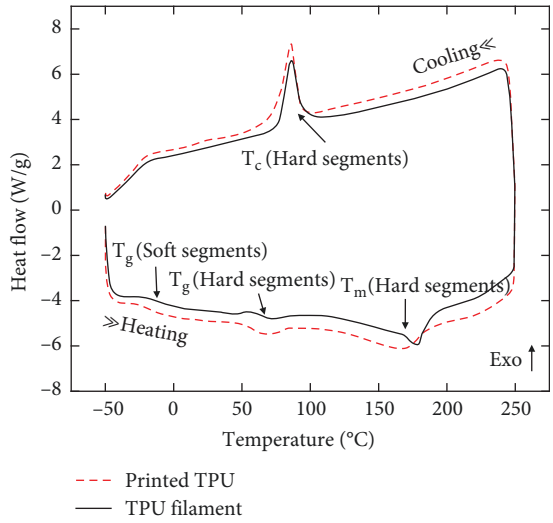

FIGURE 5: DSC curves of TPU filament and three-dimensionally printed TPU during heating and cooling processes.

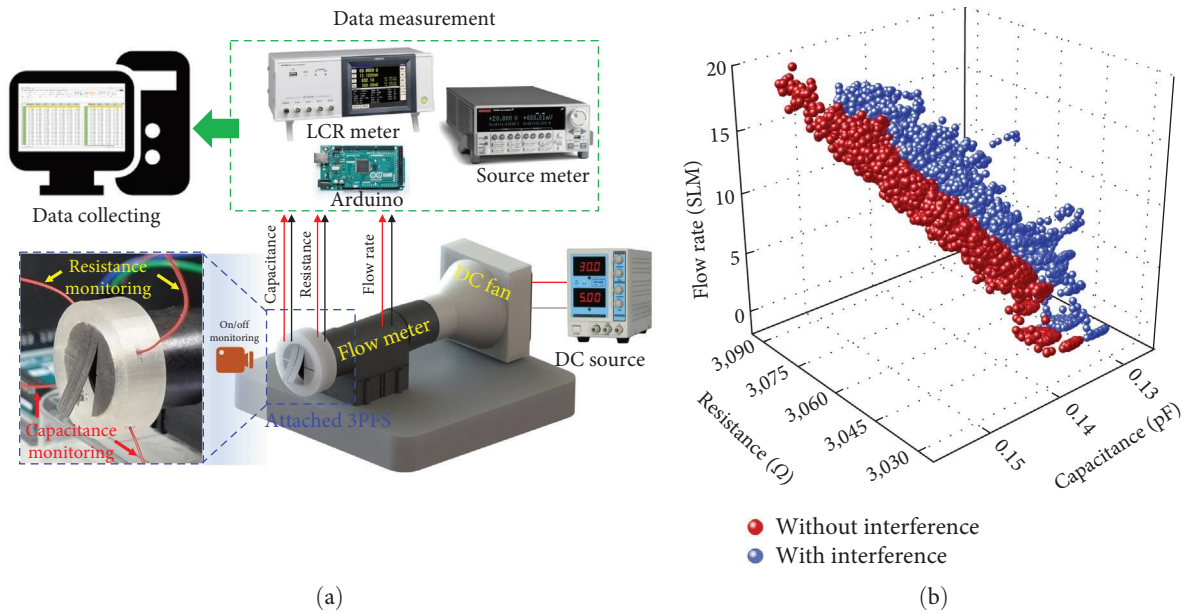

FIGURE 6: Experimental setup for dataset acquisition for model training. (a) Schematic of data collecting system comprising 3PFS, commercial flow meter, DC fan, and their measuring/controlling devices. (b) Scatter plots of obtained data points with and without external interference.

filament were evaluated to be approximately −21.3 and 72°C, respectively. Similarly, the printed TPU exhibited T_g values of approximately −23.3 and 69°C for soft and hard segments, respectively, indicating slight variations from the filament. In addition, endothermic peaks observed at approximately 175.5 and 174.6°C during the heating process correspond to the T_m for the TPU filament and printed TPU, respectively. During the cooling, a crystallization peak was consistently observed at approximately 87°C across samples. It is noteworthy that the 3D printing process affected only minor shifts, within 3°C, in all observed endothermic and exothermic peaks. Consequently, the TPU-based 3PFS can be reliably utilized within ambient temperature conditions of 5–40°C (between the two T_g points) without significant change in the mechanical properties.

4. Experimental Data Acquisition

A schematic of the experimental setup to build the 3PFS datasets is illustrated in Figure 6(a). The fabricated 3PFS was fixed to a commercial flow meter (PMF4005V, POSIFA Microsystems, Inc.) to obtain the airflow rate and corresponding resistance and capacitance changes simultaneously. In addition, the actuating performance, which depends on the flow rate, was captured using optical camera monitoring. As shown in the magnified view (see blue dotted box), the resistance and capacitance were measured using the upper and lower two wires, respectively. With the flow meter fixed to the test stage, the direct current (DC) controllable fan at the inlet generates various flow rates by randomly changing the DC voltage supply (TDP-305A, Toyotech LLC). The flow rate,

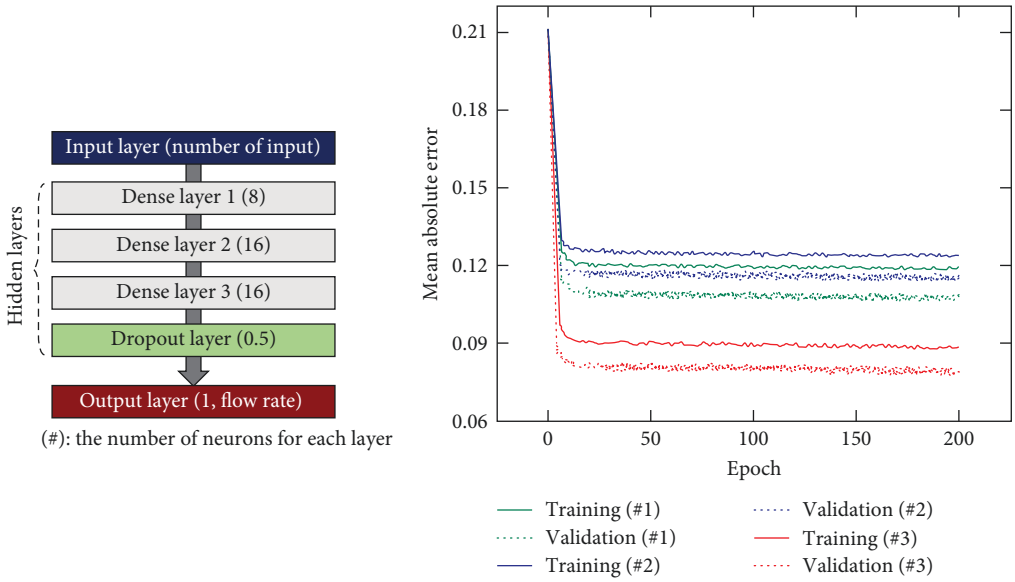

(a) (b)

FIGURE 7: (a) Illustration of DNN regression model structure with the number of nodes for flow rate prediction. (b) Training results with input cases #1, #2, and #3.

capacitance, and resistance were measured at intervals of 0.22 s using Arduino Mega 2560, inductance, capacitance, and resistance (LCR) meter (IM3536, HIOKI E.E. Corporation), and source meter (SMU 2614B, Keithley Instruments Ltd.), respectively. Finally, the evaluated data were accumulated at room temperature condition with small deviation for DNN model training.

The resistance and capacitance at the 0–19.65 SLM flow rate range (i.e., output data) were measured for the dataset. Sufficient prestretching was conducted in advance for crack-based strain sensing by inducing initial crack propagation. In the coplanar capacitance sensor, the values can be distorted by interference from other external objects affecting dielectric constant. Therefore, a commercial mobile phone and a human body were randomly placed near the 3PFS during data acquisition to consider interference affecting precise capacitance sensing in real applications. Both capacitance and resistance exhibited an increasing trend with an increasing flow rate (Figure 6(b)). However, unlike resistance, the capacitance showed a decreased value at the same flow rate by interference from the adjacent objects. In conclusion, a total of 6,965 data points, wherein 3,299 and 3,666 data points correspond to with and without interference, respectively, were successfully obtained. In addition, stepwise increasing and decreasing continuous datasets were prepared to evaluate and compare the model performances.

5. Data Preparation and DNN Model

Figure 7 shows the DNN model architecture for airflow rate prediction and training results for various input types. Python-based open-source frameworks, such as Scikit-learn, Keras, and TensorFlow, were used to realize effective data preprocessing, deep learning model configuration, and supervised learning. In addition, Google Colaboratory Pro was used as the Python cloud computing platform. For data preprocessing, input and output data were scaled between 0 and 1 using MinMaxScaler [65] through the Scikit-learn library, and the time interval was matched during the data cleaning process.

Figure 7(a) illustrates the multilayer DNN regression model with the number of neurons for airflow rate prediction. Herein, the prediction performances were compared for three conditions depending on the input cases: only capacitance, only resistance, and both (hereafter, cases #1, #2, and #3, respectively). Therefore, the unit number of the first layer was selected as one or two for single or dual inputs, respectively. The other regression layers consisted of three dense (i.e., fully connected) layers with sigmoid activation functions. Furthermore, a dropout layer [37] with a ratio of 50% was added to prevent overfitting in the training dataset. Finally, the flow rate was predicted using the 3PFS based on the electrical responses.

For algorithm training, the prepared data points were randomly split in the ratio of 7 : 1.5 : 1.5 for the training, validation, and test datasets (4,875; 1,045; and 1,045, respectively) for each repeated training. Furthermore, a mean absolute error (MAE), sigmoid, 0.01, and 200 were selected for the loss function, activation function, learning rate, and epochs, respectively. Figure 7(b) shows five average training histories with cases #1, #2, and #3 as a function of the epoch. Although the training and validation losses converged for each test dataset in all cases, case #3 exhibited a 25% and 33% decrease in validation loss compared to cases #1 and #2, respectively.

6. Results

To investigate the sensing principle of the 3PFS, optical and scanning electron microscopy (SEM) images were captured. The actuating membrane was naturally bent by airflow (Figure 8(a)). In addition, the membrane recovered its initial position (i.e., closed state) when the DC fan was turned off.

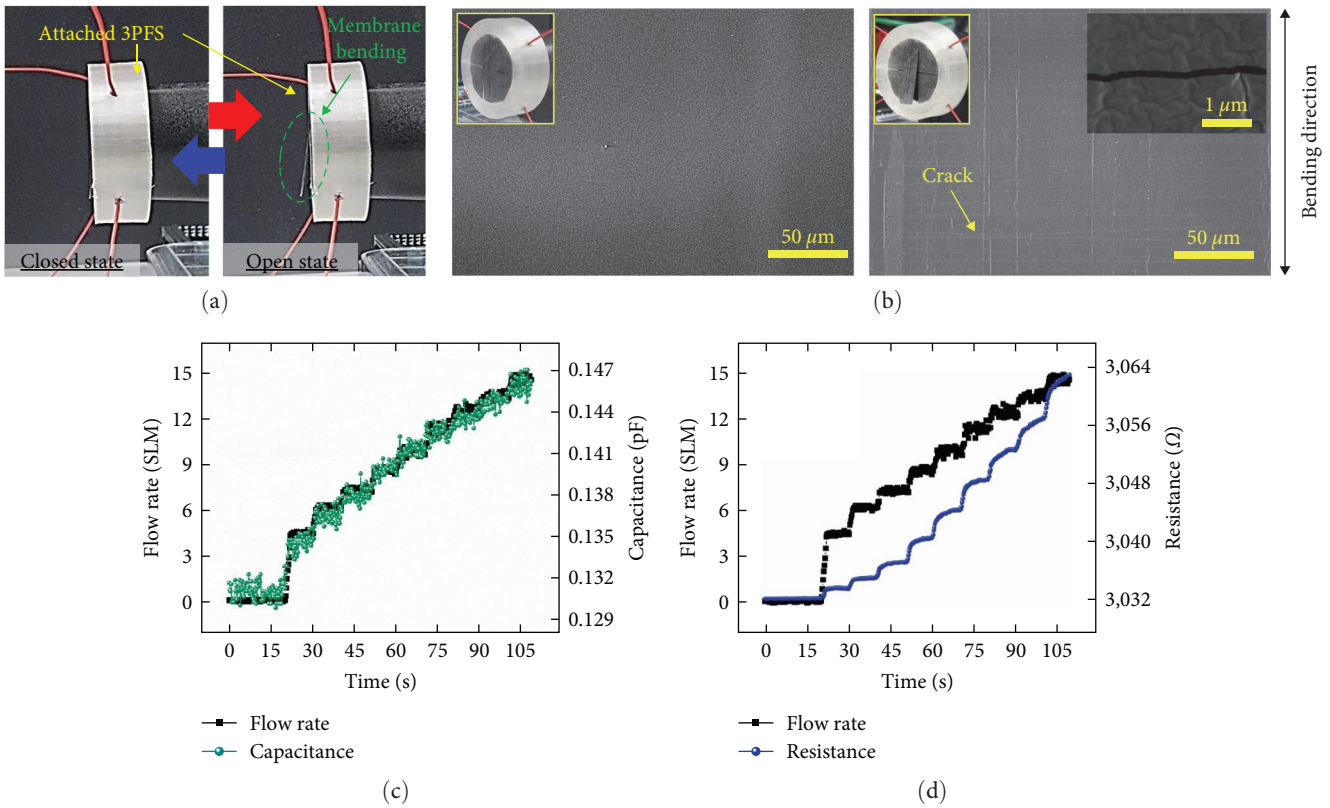

FIGURE 8: (a) Reversible movement of an actuating part by the flow rate change. (b) SEM images of Pt membrane surface at the flat (left) and bending (right) states. (c) Transient capacitance and (d) resistance response by increasing flow rate.

Thus, the flexible TPU membrane ensured a reversible sensing performance at various flow rates. Furthermore, the capacitance between the electrodes changed owing to the conductive membrane, which hinders electrical field formation. SEM images were captured (Figure 8(b)) to demonstrate the crack-based resistance change caused by the bent membrane. Compared to the initial state, the cracks were formed perpendicular to the bending direction and ensured increased resistance owing to strain. Additionally, the capacitance and resistance changes caused by the continuously increasing flow rate were evaluated, as shown in Figures 8(c) and 8(d). Although the capacitance follows a similar trend as the flow rate, a noticeable noise was observed. Furthermore, it should be noted that the coplanar capacitance is easily influenced by external interference from adjacent objects (such as the human body, electronics, and metal). Moving objects near the sensors can disrupt the electric field generated by this type of capacitance (Figure 2(c)), causing a change in capacitance value [60, 66, 67]. In contrast, the resistance signal showed disadvantages in delay time for prediction, although a similar increasing tendency was observed with low noise. The response and recovery delays occur due to the viscoelastic nature of the TPU substrate [53, 54, 68], a common characteristic of other polymer-based strain sensors. In addition, the rough surface of the 3PFS, created by 3D printing (Figure 4(b)), might affect the time delay in crack propagation and recovery. Thus, it is expected that the sensor fusion of two different data can enhance the prediction accuracy.

Figures 9(a), 9(b), and 9(c) show scatter plots of the flow rate prediction performance using the 1,045 test data points with different input conditions depending on the type of used input features (i.e., capacitance only, resistance only, and capacitance and resistance) for cases #1, #2, and #3, respectively. The predicted results (green and blue dots) were relatively distant from the actual flow rates (black line). In particular, the prediction accuracy in case #1 was lower in the entire flow range owing to external interference (Figure 9(a)). It is because noise and interference caused changes in the coplanar capacitance during the input data acquisition step, which in turn affected the accuracy of the predictions. Furthermore, inaccurate prediction results occurred under case #2 owing to the complex influence of the delay time and hysteresis of the soft material in a relatively low flow rate range (less than approximately 10 SLM; Figure 9(b)). However, in case #3, the prediction results (red dots) were relatively close to the actual value in the test range (Figure 9(c)), thus indicating improved model performance as compared to those of the single-input models.

In addition, to quantitatively compare the prediction score of the regression model, MAE, mean squared error (MSE), and root mean squared logarithmic error (RMSLE) were compared using the test dataset, which can be calculated using following equations, respectively.

$$\mathrm{MAE} = \frac{1}{n}\sum_{i=1}^{n}|y_i - p_i|, \tag{11}$$

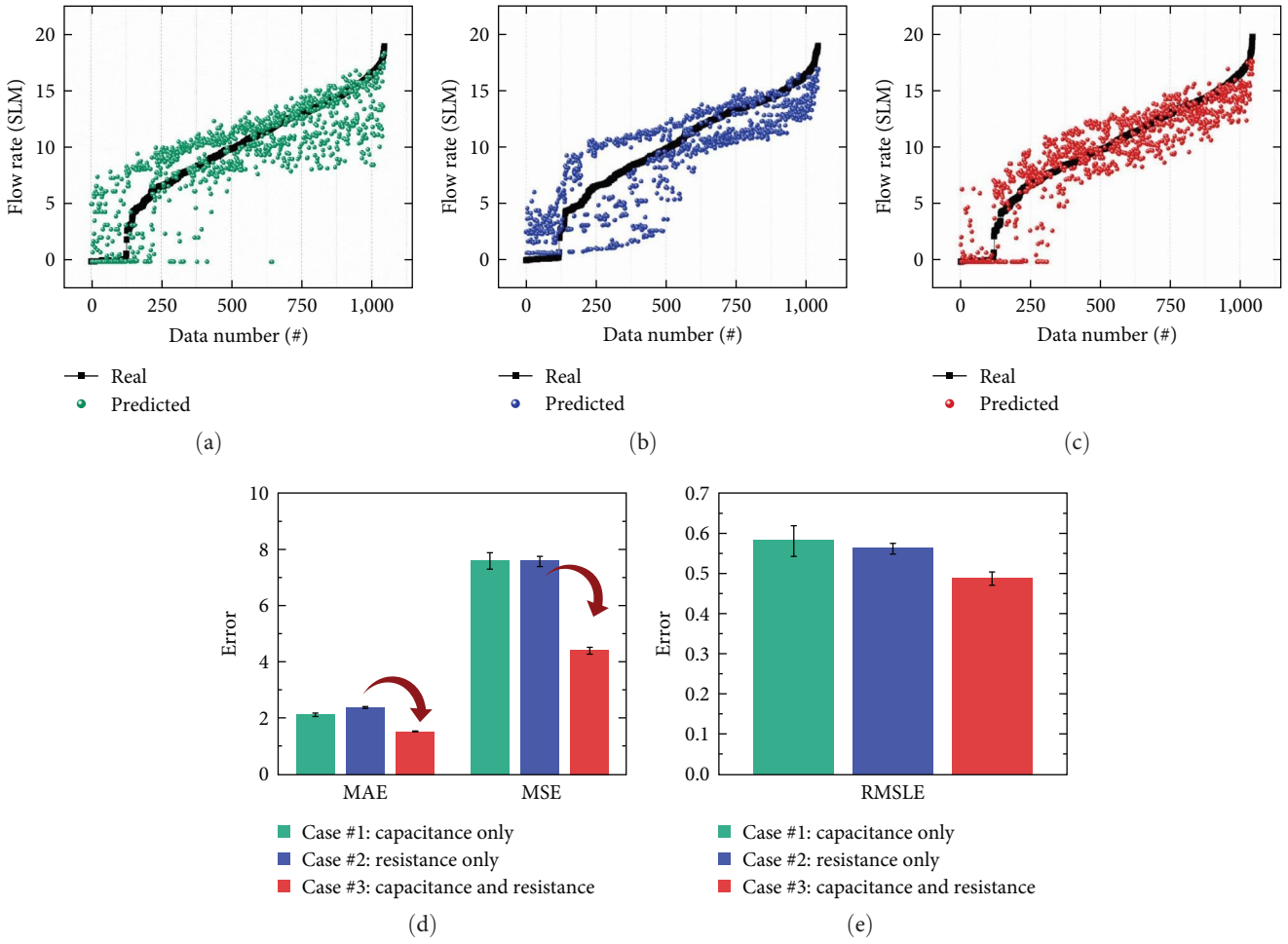

FIGURE 9: Predicting performance results using 1,045 test data points with different conditions; cases: (a) #1, (b) #2, and (c) #3. (d) Comparison of mean absolute error (MAE), mean squared error (MSE), and (e) root mean squared logarithmic error (RMSLE) of the predicted results.

$$\mathrm{MSE} = \frac{1}{n}\sum_{i=1}^{n}(y_i - p_i)^2, \tag{12}$$

$$\mathrm{RMSLE} = \sqrt{\frac{1}{n}\sum_{i=1}^{n}(\log(1+y_i) - \log(1+p_i))^2}, \tag{13}$$

where y_i, p_i, and n stand for actual value, predicted value, and the number of data points, respectively. As described in Equations (11), (12), and (13), the metrics enable the accuracy assessment of regression models. It should be noted that the final inverse-transformed flow rate values were used to evaluate the prediction performance with the metrics in the following discussion. The MAE represents the average of the absolute differences between the actual and predicted values, MSE emphasizes larger errors through squaring, and RMSLE indicates relative errors. As shown in Figure 9(d), values of 2.11 and 2.36 for MAE and 7.59 and 7.57 for MSE were obtained for cases #1 and #2, respectively. In case #3, MAE was 1.52, thus exhibiting a decrease of 27.75% and 35.51%, and MSE was 4.39, thus exhibiting a decrease of 42.16% and 42.04%, respectively, compared to cases #1 and #2. Nevertheless, case #3 exhibited enhanced prediction accuracy compared to the single-input cases. Furthermore, when utilizing the conventional linear regression model-based signal processing method of flow rate sensors [48, 69], MAE values were decreased in 29.31%, 36.25%, and 11.24% for cases #1, #2, and #3, respectively. The RMSLE also showed a relative improvement in accuracy, with a 16.11% and 13.25% decrease for case #1 and case #2, compared to case #3, as shown in Figure 9(e).

To demonstrate the potential of 3PFS for future applications, its prediction accuracy must be evaluated for continuous flow rate changes. Therefore, additional test datasets with and without external interference were conducted, and the prediction performances were compared for single and dual inputs. Figures 10(a), 10(b), and 10(c) show the test results evaluated using the test dataset without interference for cases #1, #2, and #3, respectively. When predicting the flow rate using only the capacitance signal (case #1), the output data showed different values to the real value, and significant noise was observed in the overall results. The fluctuations observed might have resulted from the original signal noise of the capacitance values in the training dataset containing interference effects being applied to the prediction of the

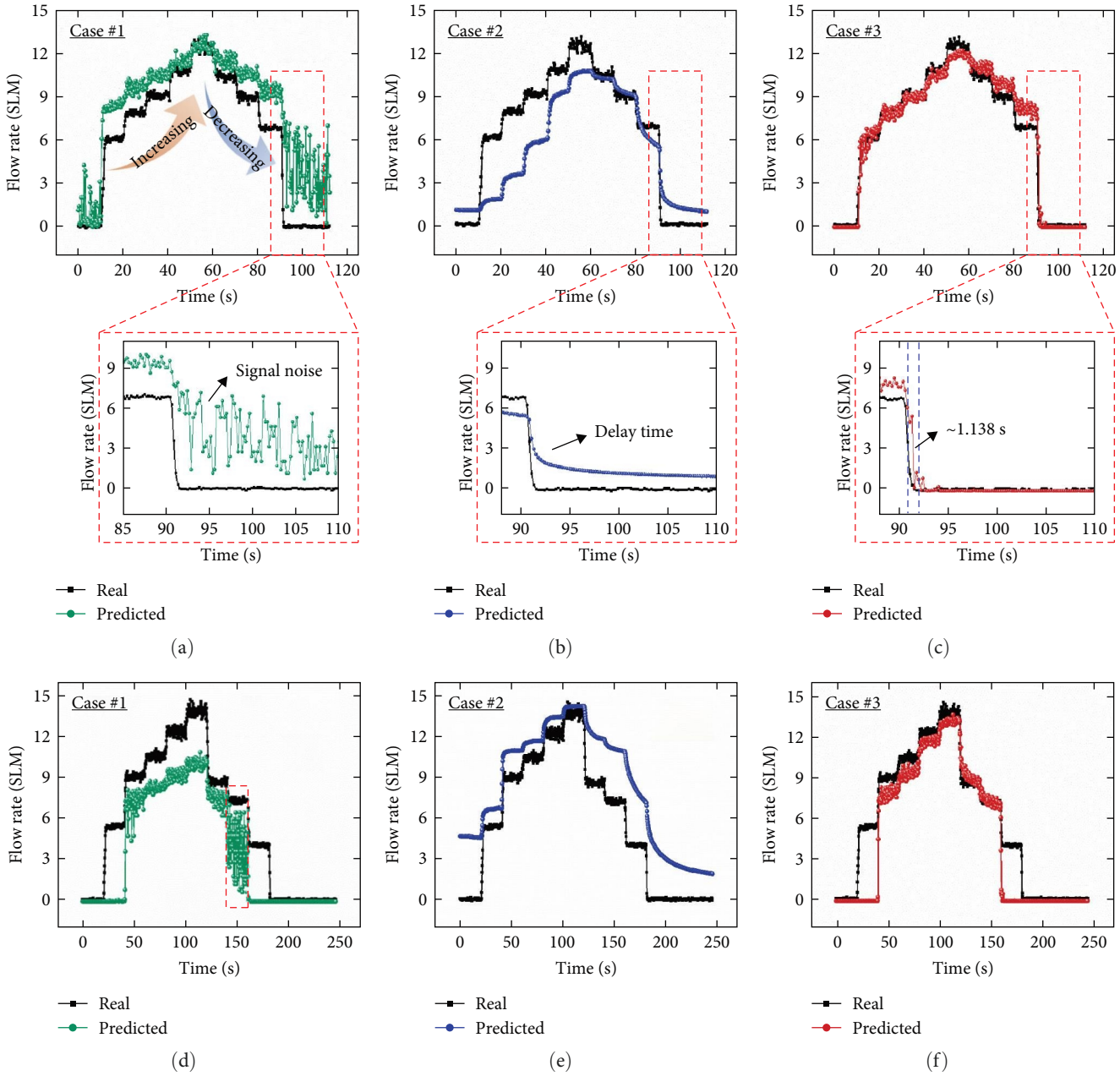

Figure 10: Continuous predicting performance comparison by applying different input conditions; cases: (a) #1, (b) #2, and (c) #3 for datasets without interference and cases: (d) #1, (e) #2, and (f) #3 for datasets with external interference.

data-driven model. In addition, the accuracy was found to be lower in the low flow rate region. Case #2 exhibited low accuracy owing to response delay of the resistance signal despite low noise. In contrast, case #3 exhibited improved prediction accuracy, with compensated noise and response delay compared to the single-input cases. As seen in the magnified plot of Figure 10, when the external flow rate is removed at ~90.5 s (~6.83 SLM), case #3 demonstrated a reduction in noise and an improved recovery time (~1.138 s) compared to cases #1 and #2, respectively.

Furthermore, trained models using the three cases (i.e., #1, #2, and #3) were investigated using another continuously increasing and decreasing flow rate dataset affected by external interference (Figures 10(d), 10(e), and 10(f)). Because the external interference decreased the overall capacitance level, the predicted results in case #1 predicted decreased values than the actual values. It can be seen from Figure 10(d) that the actual value is ~7.2 SLM at ~140–160 s, and the inaccurate prediction result is ~3.8 SLM. In addition, significant fluctuations were observed in the predicted results through the entire prediction owing to the external interference effect on the training dataset, which is a weakness of the coplanar capacitance measurement. In case #2, because the resistance signal was not directly affected by external interference, the overall prediction results showed negligible noise in the continuous signal, as shown in Figure 10(e). However,

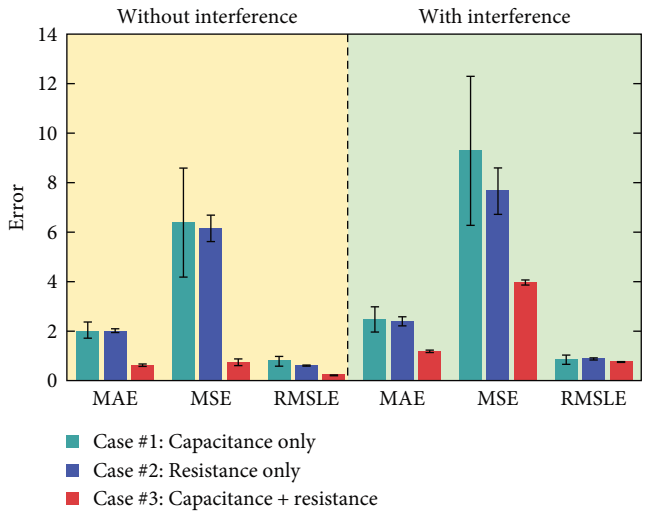

FIGURE 11: Comparison of calculated MAE, MSE, and RMSLE of the continuous response predictions with various input conditions.

the predicted values did not converge and exhibited inaccurate results because of the delay time of the fabricated resistive soft strain sensor during increasing and decreasing airflow rates. In contrast, the predicted results in case #3 showed notably enhanced sensing results compared to the single-input conditions, as depicted in Figure 10(f). In addition, considering the results in the range of 40–160 s, the predicted transient results exhibited less fluctuation in the same range than that of case #1 and rapidly converged by reducing the response time compared to case #2. Although a sensing error was observed in the low flow rate region (smaller than ~5.3 SLM), the accuracy can be enhanced by a reinforced dataset considering low flow rate cases and improving the DNN architecture with advanced training algorithms. These results demonstrate that dual input sensor fusion can enhance prediction performance by eliminating the disadvantages of individual electrical signal features.

Furthermore, the results in Figure 10 were compared by calculating regression metrics using Equations (11), (12), and (13) from the differences between the predicted and actual values according to the various input cases for continuous 491 and 1,080 test data points of both conditions, respectively. The average MAE, MSE, and RMSLE of five different training results with the newly shuffled datasets were calculated to characterize the sensing results of the continuous test datasets quantitatively. The MAE, MSE, and RMSLE from the DNN model applying case #3 were evaluated as 0.59, 0.7, and 0.18 for continuous test datasets without interference and 1.16, 3.95, and 0.73 with interference, respectively (Figure 11). Therefore, the developed model using sensor fusion demonstrated a good prediction performance with a small deviation from the actual flow rate, few outliers, and low relative error as evident from the low MAE, MSE, and RMSLE values. Moreover, the error values of case #3 were much smaller than those of cases #1 and #2 in all evaluations. In the absence of external interference, case #3 showed decreased MAE, MSE, and RMSLE of ~70.37%, 88.74%, and 72.26% on average, respectively, compared with cases #1 and #2. Furthermore, using the test dataset with interference, a 51.91%, 53.01%, and 12.20% decrease in MAE, MSE, and RMSLE, respectively, were exhibited compared to cases #1 and #2 on average. Although the difference between MAE and MSE increased owing to the prediction error in the low flow rate region, sensor fusion improves the sensing performance. Consequently, for data-driven DNN regression models with a single input, the predicted output results reflect and depend on the characteristics of the initial responses. In addition, R2 scores for the test datasets with and without interference were evaluated as 0.6736 and 0.6065 for case #1 on average, respectively. For case #2, the scores were 0.6854 and 0.6762, respectively. In contrast, case #3 showed relatively improved values of 0.9639 and 0.8331 for each test dataset. Thus, various input combinations via sensor fusion can reduce sensing errors and enhance the prediction performance. In summary, the DNN-assisted 3PFS is an accurate flow rate sensing system that simultaneously uses multiple electrical properties as input features. Notably, the novel sensing system can overcome the disadvantages of capacitances (e.g., signal noise and external interference) and resistance (e.g., delay time) sensing for reliable and stable results.

To confirm the long-term reliability of the proposed 3PFS, the temperature stability of the TPU material and mechanical durability of the actuating membrane should be also demonstrated. Therefore, the signal changes were measured under harsh conditions considering wind power system environments [70, 71] such as temperature (5–40°C) and airflow cycles. Figure 12(a) shows the normalized resistance change in the strain-sensing region in response to the dynamic temperature changes. The 3PFS was subjected to 68 temperature cycles between 5 and 40°C (dotted line) using a temperature-controlled chamber (THMS600PS, Linkam Scientific Instruments Ltd.) with a temperature change rate of 20°C/min and a maintaining time of 7 min at each saturated temperature. During the ~20-hr durability test, the normalized resistance values exhibited an almost identical trend, confirming the operational stability of the 3PFS under simulated wind power system conditions. However, it should be noted that future compensation will be necessary according to the ambient temperature and the temperature coefficient of resistance (TCR) of the conductive region. Furthermore, to assess the mechanical durability of the moving part, a 720 cycle test was conducted. As depicted in Figure 12(b), the test condition involved switching between "on" mode (~12.2 SLM) and "off" mode at 5-s intervals using a relay switch module. As a result, the normalized resistance response exhibited the consistent trends across 720 cycles. Although the rate of change was maintained, a deviation in the base signal was observed due to the influence of ambient temperature, indicating that additional sensor packaging may be required for more robust operation in real-world applications.

7. Discussion

Table 1 presents the fabrication, type, material, performance, and test conditions of flow sensors from recent literature compared to this work. Yi et al. [72] utilized a photolithography

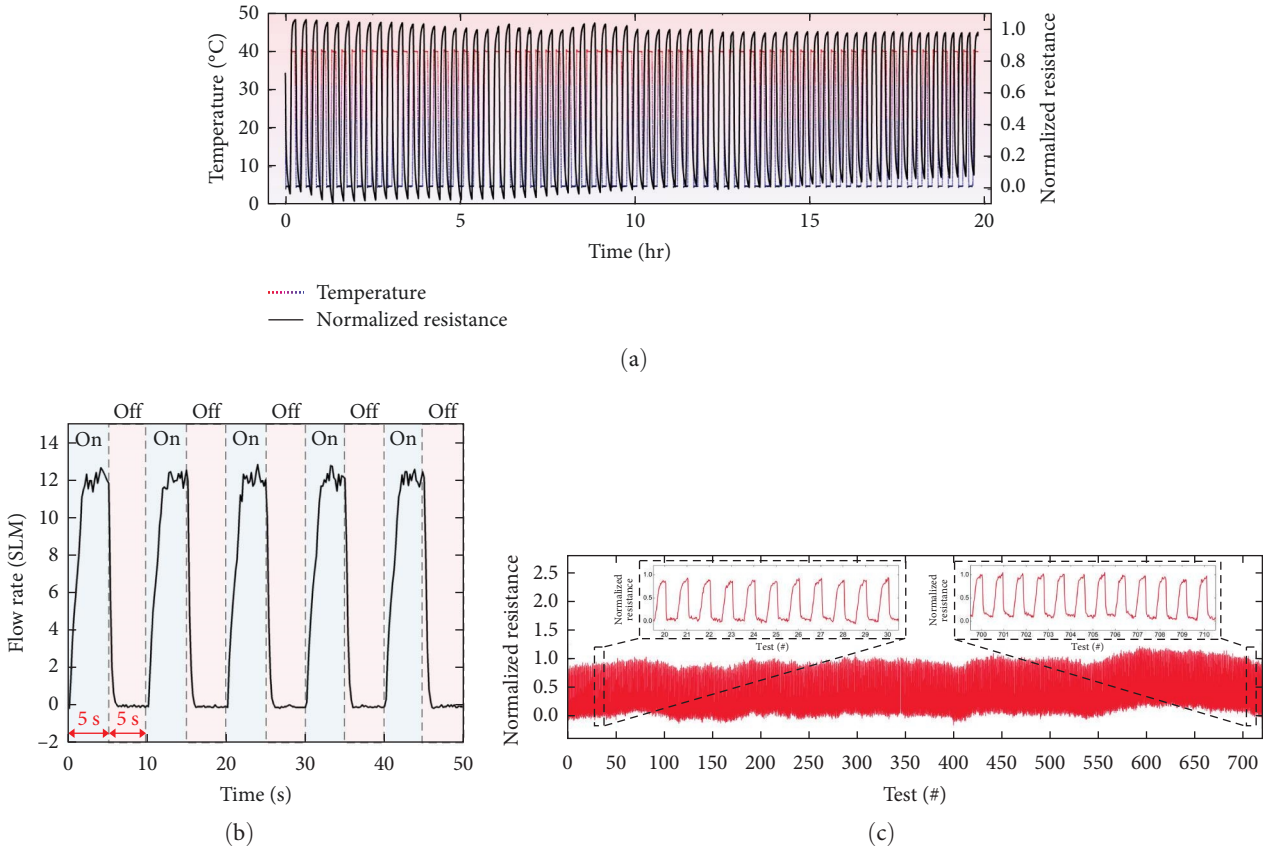

Figure 12: Durability tests of 3PFS with different environmental conditions: (a) temperature change, (b) repeatedly applied flow rate condition, and (c) the resistance change.

process to fabricate thermal flow sensors, achieving a relative error of less than 14% in voltage output. In addition, Xu et al. [73] and Qi et al. [75] proposed temperature effect compensation methods under varying ambient temperature conditions. Haneda et al. [74] applied a DNN model to convert the signals from three MEMS-based differential pressure sensors into wind speed, achieving a root MSE value of 0.24 m/s.

However, MEMS-based sensor fabrications require high-cost equipment, materials, and the use of toxic solutions, as detailed in Table S1. Therefore, 3D printing-based wind sensors have been adopted to substitute the conventional method due to their scalability, large-scale production, time, and cost efficiency for sustainable development. Recently, 3D printing-assisted sensors based on thermal or strain-sensing principles have been developed using conductive or flexible filaments. Daniel et al. [48] proposed a completely 3D-printed thermal anemometer, although it exhibited unstable outputs during repeated trials. In addition, a strain-based flow sensor developed by AI-Rubaiai et al. [76] showed initial resistance changes during a 1000 cycle test. Meanwhile, Ye et al. [77] applied 3D printing techniques to induce fluid-structure interaction, measuring the deformation with a commercial strain gauge and achieving low error results. This work introduces a novel fabrication method using 3D printing for multiple sensing and thermal/mechanical durability tests. Furthermore, a DNN-based signal processing offers a promising method for enhanced airflow measurement and future reliable wind power systems.

While the 3PFS can predict the airflow rate with high accuracy and cost-effective measurements, further discussions are needed for the real applications. Firstly, due to the TCR of metal region, an overall shift can occur in environments with very high ambient temperatures. Therefore, the sensing performance needs verification for the additional calibrations under different fluid types and temperatures. In addition, as shown in previous research [78], components that respond independently of temperature can be utilized to decouple the thermal effect. To address the known limitation of data-driven models, it is crucial to obtain a large number of data points uniformly that fit the range of the intended application environments. It should be noted that utilizing a DNN-based pretrained model in this study allows for ease of real-world applications with small data points through another advanced deep learning approach including domain adaptation [79] and transfer learning [80] methods. Therefore, training the model with datasets considering the real application environments, such as temperature or external interference, can further increase the accuracy. However, the proposed 3PFS showed cost-effective and eco-friendly fabrication methods compared to the conventional approaches (Table S1) for the multiple sensing principles with accurate flow rate sensing performance using DNN model.

Table 1: Comparison of recent studies for various flow sensors.

Ref	Year	Core fabrication	Sensor type	Material	Fluid type	Accuracy	Durability
[72]	2019	Microfabrication	Thermal	Ni, Al, SiO_2, and Si	Air	Relative error: less than 14%	—
[73]	2019	Microfabrication	Thermal	Poly Si, Si, and PMMA	Air (N_2)	—	22–48°C
[74]	2023	Microfabrication	DP	Au, Si, and SiO_2	Air	RMSE: 0.24 m/s	—
[75]	2024	Microfabrication	Thermal	Ti, Pt, Au, and ceramic	Air	Maximum error: 1.027 m/s	0–40°C
[48]	2020	3D printing	Thermal	Conductive PLA and ABS	Air (N_2)	Sensitivity: $0.059 \pm 0.010\,\text{sccm}^{-1}$	Three trials
[76]	2019	3D printing	Strain	Conductive TPU	Air	—	1,000 cycles
[77]	2022	3D printing	Strain	Metal and PLA	Air	Maximum error: 0.87 m/s	—
This work	2024	3D printing	Strain and capacitance	Pt and TPU	Air	MAE: 0.59 SLM	5–40°C 720 cycles

PLA, polylactic acid; DP, differential pressure; RMSE, root mean square error; Poly Si, polycrystalline silicon; PMMA, polymethyl methacrylate.

8. Conclusion

In conclusion, a facile and novel manufacturing and measuring method for a flow rate sensing system was demonstrated using 3D printing technology and a data-driven DNN. Owing to the additive manufacturing and deep learning models, ease of fabrication, sensor fusion, and enhanced sensing performance were realized. In addition, the principle of coplanar capacitance and crack-based resistance change of 3PFS due to the actuating membrane by airflows was demonstrated using actuation monitoring and captured SEM images. Subsequently, the prediction performance of the trained DNN models was compared for various input conditions (i.e., capacitance (case #1), resistance (case #2), and both features (case #3)) using experimentally acquired 6,965 datasets considering the external interference from the external objects affecting dielectric constant. Case #3 exhibited enhanced performance in terms of prediction accuracy with relatively low signal noise and delay time compared to cases #1 and #2. In particular, for the transient test dataset without external interference, the MAE, MSE, and RMSLE were decreased by 70.37%, 88.74%, and 72.26%, respectively. In addition, MAE, MSE, and RMSLE decreased by 51.91%, 53.01%, and 12.20% with the interference. The results suggest that quantitative prediction error was significantly reduced as the disadvantages of noisy signals and response delay from single inputs were simultaneously minimized. In summary, by using 3PFS, which can gather two different signals, the limitations of the results obtained with only one sensor were overcome, and the performance was significantly improved through sensor fusion. The findings of this study will enlarge reliable sensing applications by applying deep learning to various wind power systems and factories.

Data Availability

The data that support the findings of this study are available from the corresponding author upon reasonable request.

Conflicts of Interest

The authors declare that they have no conflicts of interest.

Acknowledgments

This work was supported by the Korea Institute of Energy Technology Evaluation and Planning (KETEP) and the Ministry of Trade, Industry, and Energy (MOTIE) of the Republic of Korea (No. 20221A1010001B and 20202000000010).

Supplementary Materials

Supplementary materials of design parameters and costs of 3PFS. (*Supplementary Materials*)

References

[1] N. Mohammed and M. M. Ali, "Optimal sizing of hybrid renewable energy system using two-stage stochastic programming," *International Journal of Energy Research*, vol. 2024, Article ID 2361858, 20 pages, 2024.

[2] M. M. Mahmoud, H. S. Salama, M. Bajaj et al., "Integration of wind systems with SVC and STATCOM during various events to achieve FRT capability and voltage stability: towards the reliability of modern power systems," *International Journal of Energy Research*, vol. 2023, Article ID 8738460, 28 pages, 2023.

[3] V. D. P. I. E. Koung, F. D. Menga, B. Bonoma, J. L. Nsouandele, and R. M. Mouangue, "Technoeconomic analysis of a wind power generation system and wind resource mapping using GIS tools: the case of twelve locations in the commune of evodoula, Cameroon," *International Journal of Energy Research*, vol. 2024, Article ID 8825472, 61 pages, 2024.

[4] S. Nechausov, A. Ivanchenko, O. Morozov et al., "Effects of ionic liquids and dual curing on vat photopolymerization process and properties of 3d-printed ionogels," *Additive Manufacturing*, vol. 56, Article ID 102895, 2022.

[5] X. An, Y. Mu, J. Liang, J. Li, Y. Zhou, and X. Sun, "Stereolithography 3D printing of ceramic cores for hollow aeroengine turbine blades," *Journal of Materials Science & Technology*, vol. 127, pp. 177–182, 2022.

[6] R. F. Quero, B. M. de C. Costa, J. A. F. da Silva, and D. P. de Jesus, "Using multi-material fused deposition modeling (FDM) for one-step 3D printing of microfluidic capillary electrophoresis with integrated electrodes for capacitively coupled contactless conductivity detection," *Sensors and Actuators B: Chemical*, vol. 365, Article ID 131959, 2022.

[7] Y. Yang, Y. Chen, Y. Wei, and Y. Li, "3D printing of shape memory polymer for functional part fabrication," *The International Journal of Advanced Manufacturing Technology*, vol. 84, pp. 2079–2095, 2016.

[8] K. Kim, J. Park, J. Suh, M. Kim, Y. Jeong, and I. Park, "3D printing of multiaxial force sensors using carbon nanotube (CNT)/thermoplastic polyurethane (TPU) filaments," *Sensors and Actuators A: Physical*, vol. 263, pp. 493–500, 2017.

[9] S. Song, Y. Li, Q. Wang, and C. Zhang, "Boosting piezoelectric performance with a new selective laser sintering 3D printable PVDF/graphene nanocomposite," *Composites Part A: Applied Science and Manufacturing*, vol. 147, Article ID 106452, 2021.

[10] P. Kulinowski, P. Malczewski, E. Pesta et al., "Selective laser sintering (SLS) technique for pharmaceutical applications—development of high dose controlled release printlets," *Additive Manufacturing*, vol. 38, Article ID 101761, 2021.

[11] X. Kuang, J. Wu, K. Chen et al., "Grayscale digital light processing 3D printing for highly functionally graded materials," *Science Advances*, vol. 5, no. 5, pp. 1–10, 2019.

[12] D. K. Patel, A. H. Sakhaei, M. Layani, B. Zhang, Q. Ge, and S. Magdassi, "Highly stretchable and UV curable elastomers for digital light processing based 3D printing," *Advanced Materials*, vol. 29, no. 15, Article ID 1606000, 2017.

[13] S. Kouchakzadeh and K. Narooei, "Simulation of piezoresistance and deformation behavior of a flexible 3D printed sensor considering the nonlinear mechanical behavior of materials," *Sensors and Actuators A: Physical*, vol. 332, Article ID 113214, 2021.

[14] C. Kalinke, P. R. de Oliveira, B. C. Janegitz, and J. A. Bonacin, "Prussian blue nanoparticles anchored on activated 3D printed sensor for the detection of L-cysteine," *Sensors and Actuators B: Chemical*, vol. 362, Article ID 131797, 2022.

[15] S. Waheed, J. M. Cabot, N. P. Macdonald et al., "3D printed microfluidic devices: enablers and barriers," *Lab on A Chip*, vol. 16, no. 11, pp. 1993–2013, 2016.

[16] A. A. Yazdi, A. Popma, W. Wong, T. Nguyen, Y. Pan, and J. Xu, "3D printing: an emerging tool for novel microfluidics

and lab-on-a-chip applications," *Microfluidics and Nanofluidics*, vol. 20, no. 3, Article ID 50, 2016.

[17] A. Kotikian, R. L. Truby, J. W. Boley, T. J. White, and J. A. Lewis, "3D printing of liquid crystal elastomeric actuators with spatially programed nematic order," *Advanced Materials*, vol. 30, no. 10, Article ID 1706164, 2018.

[18] Y-Fang Zhang, N. Zhang, H. Hingorani et al., "Fast-response, stiffness-tunable soft actuator by hybrid multimaterial 3D printing," *Advanced Functional Materials*, vol. 29, no. 15, Article ID 1806698, 2019.

[19] M. Schaffner, J. A. Faber, L. Pianegonda, P. A. Rühs, F. Coulter, and A. R. Studart, "3D printing of robotic soft actuators with programmable bioinspired architectures," *Nature Communications*, vol. 9, no. 1, Article ID 878, 2018.

[20] V. Jašo, M. V. Rodić, and Z. S. Petrović, "Biocompatible fibers from thermoplastic polyurethane reinforced with polylactic acid microfibers," *European Polymer Journal*, vol. 63, pp. 20–28, 2015.

[21] M. Tiboni, R. Campana, E. Frangipani, and L. Casettari, "3D printed clotrimazole intravaginal ring for the treatment of recurrent vaginal candidiasis," *International Journal of Pharmaceutics*, vol. 596, Article ID 120290, 2021.

[22] G. Scetta, N. Selles, P. Heuillet, M. Ciccotti, and C. Creton, "Cyclic fatigue failure of TPU using a crack propagation approach," *Polymer Testing*, vol. 97, Article ID 107140, 2021.

[23] L.-Y. Zhou, J. Fu, and Y. He, "A review of 3D printing technologies for soft polymer materials," *Advanced Functional Materials*, vol. 30, no. 28, Article ID 2000187, 2020.

[24] S. Han, T. Kim, D. Kim, Y.-L. Park, and S. Jo, "Use of deep learning for characterization of microfluidic soft sensors," *IEEE Robotics and Automation Letters*, vol. 3, pp. 873–880, 2018.

[25] Y.-L. Park, D. Tepayotl-Ramirez, R. J. Wood, and C. Majidi, "Influence of cross-sectional geometry on the sensitivity and hysteresis of liquid-phase electronic pressure sensors," *Applied Physics Letters*, vol. 101, no. 19, Article ID 191904, 2012.

[26] Y.-L. Park, C. Majidi, R. Kramer, P. Bérard, and R. J. Wood, "Hyperelastic pressure sensing with a liquid-embedded elastomer," *Journal of Micromechanics and Microengineering*, vol. 20, no. 12, Article ID 125029, 2010.

[27] T. Chen, T. Xiang, T. Lei, and M. Xu, "Deep learning for the design of toroidal metasurfaces," *IEEE Photonics Journal*, vol. 15, no. 2, pp. 1–7, 2023.

[28] S. M. Rezaeinia, R. Rahmani, A. Ghodsi, and H. Veisi, "Sentiment analysis based on improved pre-trained word embeddings," *Expert Systems with Applications*, vol. 117, pp. 139–147, 2019.

[29] H. Palangi, L. Deng, Y. Shen et al., "Deep sentence embedding using long short-term memory networks: analysis and application to information retrieval," *IEEE/ACM Transactions on Audio, Speech, and Language Processing*, vol. 24, no. 4, pp. 694–707, 2016.

[30] A. Brunetti, D. Buongiorno, G. F. Trotta, and V. Bevilacqua, "Computer vision and deep learning techniques for pedestrian detection and tracking: a survey," *Neurocomputing*, vol. 300, pp. 17–33, 2018.

[31] X. Wu, D. Sahoo, and S. C. H. Hoi, "Recent advances in deep learning for object detection," *Neurocomputing*, vol. 396, pp. 39–64, 2020.

[32] C. De Vente, P. Vos, M. Hosseinzadeh, J. Pluim, and M. Veta, "Deep learning regression for prostate cancer detection and grading in Bi-parametric MRI," *IEEE Transactions on Biomedical Engineering*, vol. 68, pp. 374–383, 2021.

[33] S. Shin, B. Ko, and H. So, "Noncontact thermal mapping method based on local temperature data using deep neural network regression," *International Journal of Heat and Mass Transfer*, vol. 183, Article ID 122236, 2022.

[34] S. Feng, H. Zhou, and H. Dong, "Using deep neural network with small dataset to predict material defects," *Materials & Design*, vol. 162, pp. 300–310, 2019.

[35] Y. Yang, J. Sun, H. Li, and Z. Xu, "ADMM-CSNet: a deep learning approach for image compressive sensing," *IEEE Transactions on Pattern Analysis and Machine Intelligence*, vol. 42, pp. 521–538, 2020.

[36] S. U. Yunas and K. B. Ozanyan, "Gait activity classification using multi-modality sensor fusion: a deep learning approach," *IEEE Sensors Journal*, vol. 21, no. 15, pp. 16870–16879, 2021.

[37] M. K. Al-Sharman, Y. Zweiri, M. A. K. Jaradat, R. Al-Husari, D. Gan, and L. D. Seneviratne, "Deep-learning-based neural network training for state estimation enhancement: application to attitude estimation," *IEEE Transactions on Instrumentation and Measurement*, vol. 69, pp. 24–34, 2020.

[38] H. Yi and K.-H. N. Bui, "An automated hyperparameter search-based deep learning model for highway traffic prediction," *IEEE Transactions on Intelligent Transportation Systems*, vol. 22, no. 9, pp. 5486–5495, 2021.

[39] F. Ejeian, S. Azadi, A. Razmjou et al., "Design and applications of MEMS flow sensors: a review," *Sensors and Actuators A: Physical*, vol. 295, pp. 483–502, 2019.

[40] Y.-H. Wang, C.-P. Chen, C.-M. Chang et al., "MEMS-based gas flow sensors," *Microfluidics and Nanofluidics*, vol. 6, no. 3, pp. 333–346, 2009.

[41] R. E. Oosterbroek, T. S. J. Lammerink, J. W. Berenschot, G. J. M. Krijnen, M. C. Elwenspoek, and A. van den Berg, "A micromachined pressure/flow-sensor," *Sensors and Actuators A: Physical*, vol. 77, no. 3, pp. 167–177, 1999.

[42] M. A. Boillat, A. J. van der Wiel, A. C. Hoogerwerf, and N. F. de Rooij, "A differential pressure liquid flow sensor for flow regulation and dosing systems," *Micro Electro Mechanical Systems*, Article ID 350, 1995.

[43] C.-L. Wei, C.-F. Lin, and I.-T. Tseng, "A novel MEMS respiratory flow sensor," *IEEE Sensors Journal*, vol. 10, no. 1, pp. 16–18, 2010.

[44] Q. Zhang, W. Ruan, H. Wang, Y. Zhou, Z. Wang, and L. Liu, "A self-bended piezoresistive microcantilever flow sensor for low flow rate measurement," *Sensors and Actuators A: Physical*, vol. 158, no. 2, pp. 273–279, 2010.

[45] S. D. Nguyen, I. Paprotny, P. K. Wright, and R. M. White, "MEMS capacitive flow sensor for natural gas pipelines," *Sensors and Actuators A: Physical*, vol. 231, pp. 28–34, 2015.

[46] S.-H. Liao, W.-J. Chen, and M. S. C. Lu, "A CMOS MEMS capacitive flow sensor for respiratory monitoring," *IEEE Sensors Journal*, vol. 13, no. 5, pp. 1401-1402, 2013.

[47] S. Shin, G. Park, W.-Y. Kim, and H. So, "A hybrid fabrication technique of capacitive flow meters using three-dimensional printing for rectifying airflows," *IEEE Access*, vol. 10, pp. 45073–45079, 2022.

[48] F. Daniel, J. Peyrefitte, and A. D. Radadia, "Towards a completely 3D printed hot wire anemometer," *Sensors and Actuators A: Physical*, vol. 309, Article ID 111963, 2020.

[49] H. Wang, M. Zhang, and Y. Yang, "Machine learning for multiphase flowrate estimation with time series sensing data," *Measurement: Sensors*, vol. 10–12, Article ID 100025, 2020.

[50] M. Manami, S. Seddighi, and R. Örlü, "Deep learning models for improved accuracy of a multiphase flowmeter," *Measurement*, vol. 206, Article ID 112254, 2023.

[51] H. Harija, B. George, and A. K. Tangirala, "A cantilever-based flow sensor for domestic and agricultural water supply system," *IEEE Sensors Journal*, vol. 21, no. 23, pp. 27147–27156, 2021.

[52] Z. Zhang, Y. Kang, N. Yao et al., "A multifunctional airflow sensor enabled by optical micro/nanofiber," *Advanced Fiber Materials*, vol. 3, no. 6, pp. 359–367, 2021.

[53] T. Nguyen, M. Chu, R. Tu, and M. Khine, "The effect of encapsulation on crack-based wrinkled thin film soft strain sensors," *Materials*, vol. 14, no. 2, Article ID 364, 2021.

[54] M. Amjadi, K.-U. Kyung, I. Park, and M. Sitti, "Stretchable, skin-mountable, and wearable strain sensors and their potential applications: a review," *Advanced Functional Materials*, vol. 26, no. 11, pp. 1678–1698, 2016.

[55] A. M. Kamat, X. Zheng, B. Jayawardhana, and A. G. P. Kottapalli, "Bioinspired PDMS-graphene cantilever flow sensors using 3D printing and replica moulding," *Nanotechnology*, vol. 32, no. 9, Article ID 095501, 2020.

[56] M. Mwelango, T. Zhu, K. Wen et al., "Coplanar capacitive sensors and their applications in non-destructive evaluation: a review," *Nondestructive Testing and Evaluation*, vol. 38, no. 5, pp. 861–905, 2023.

[57] N. Li, H. Zhu, W. Wang, and Y. Gong, "Parallel double-plate capacitive proximity sensor modelling based on effective theory," *AIP Advances*, vol. 4, no. 2, Article ID 027119, 2014.

[58] J. Z. Chen, A. A. Darhuber, S. M. Troian, and S. Wagner, "Capacitive sensing of droplets for microfluidic devices based on thermocapillary actuation," *Lab on A Chip*, vol. 4, no. 5, pp. 473–480, 2004.

[59] M. F. A. Rahman, M. N. M. Nawi, A. A. Manaf, M. R. Arshad, and O. Sidek, "Validation of finite element model (FEM) of coplanar electrodes capacitive sensing using microfluidic-based sensor device," in *2013 Fifth International Conference on Computational Intelligence, Communication Systems and Networks*, pp. 409–413, IEEE, Madrid, Spain, August 2013.

[60] N. Li, M. Cao, X. Yu, J. Jia, and Y. Yang, "High sensitive capacitive sensing method for thickness detection of the water film on an insulation surface," *IEEE Access*, vol. 7, pp. 96384–96391, 2019.

[61] B. N. Ntamba and V. Fester, "Pressure losses and limiting reynolds numbers for non-newtonian fluids in short square-edged orifice plates," *Journal of Fluids Engineering*, vol. 134, no. 9, pp. 1–9, 2012.

[62] S. Vemulapalli and S. K. Venkata, "Parametric analysis of orifice plates on measurement of flow: a review," *Ain Shams Engineering Journal*, vol. 13, no. 3, Article ID 101639, 2022.

[63] A. Frick and A. Rochman, "Characterization of TPU-elastomers by thermal analysis (DSC)," *Polymer Testing*, vol. 23, no. 4, pp. 413–417, 2004.

[64] A. Saiani, A. Novak, L. Rodier, G. Eeckhaut, J.-W. Leenslag, and J. S. Higgins, "Origin of multiple melting endotherms in a high hard block content polyurethane: effect of annealing temperature," *Macromolecules*, vol. 40, no. 20, pp. 7252–7262, 2007.

[65] S. K. Dey, A. Hossain, and M. M. Rahman, "Implementation of a web application to predict diabetes disease," in *2018 21st International Conference of Computer and Information Technology (ICCIT)*, pp. 1–5, IEEE, Dhaka, Bangladesh, December 2018.

[66] P. Makireddy and P. Vooka, "A comparison-based interface circuit for detection of motion direction of humans using capacitive sensor," *IEEE Sensors Journal*, vol. 23, no. 23, pp. 29063–29072, 2023.

[67] R. Moheimani, P. Hosseini, S. Mohammadi, and H. Dalir, "Recent advances on capacitive proximity sensors: from design and materials to creative applications," *C—Journal of Carbon Research*, vol. 8, no. 2, Article ID 26, 2022.

[68] D. Wang, G. de Boer, A. Neville, and A. Ghanbarzadeh, "A review on modelling of viscoelastic contact problems," *Lubricants*, vol. 10, no. 12, Article ID 358, 2022.

[69] S. Issa and W. Lang, "Minimum detectable air velocity by thermal flow sensors," *Sensors*, vol. 13, no. 8, pp. 10944–10953, 2013.

[70] K. Fischer, M. Steffes, K. Pelka, B. Tegtmeier, and M. Dörenkämper, "Humidity in power converters of wind turbines—field conditions and their relation with failures," *Energies*, vol. 14, no. 7, Article ID 1919, 2021.

[71] S.-C. Wu, J.-C. Tzou, and C.-Y. Ding, "A low-cost system for measuring wind speed and direction using thermopile array and artificial neural network," *Applied Sciences*, vol. 11, no. 9, Article ID 4024, 2021.

[72] Z. Yi, Y. Ye, M. Qin, and Q.-A. Huang, "Modeling of packaged MEMS thermal wind sensor operating on CP mode," *IEEE Transactions on Electron Devices*, vol. 66, pp. 2375–2381, 2019.

[73] W. Xu, S. Ma, X. Wang, Y. Chiu, and Y.-K. Lee, "A CMOS-MEMS thermoresistive micro calorimetric flow sensor with temperature compensation," *Journal of Microelectromechanical Systems*, vol. 28, pp. 841–849, 2019.

[74] K. Haneda, K. Matsudaira, and H. Takahashi, "Neural network-based airflow vector sensor using multiple MEMS differential pressure sensors," *IEEE Access*, vol. 11, pp. 40978–40987, 2023.

[75] B. Qi, Z. Yi, M. Qin, and Q.-A. Huang, "Novel temperature drift compensation for MEMS thermal wind sensors by heating power calibration circuits," *IEEE Transactions on Instrumentation and Measurement*, vol. 73, pp. 1–9, 2024.

[76] M. Al-Rubaiai, R. Tsuruta, U. Gandhi, C. Wang, and X. Tan, "A 3D-printed stretchable strain sensor for wind sensing," *Smart Materials and Structures*, vol. 28, no. 8, Article ID 084001, 2019.

[77] Y. Ye, S. Wan, S. Li, and X. He, "Mechanical wind sensor based on additive manufacturing technology," *IEEE Transactions on Instrumentation and Measurement*, vol. 71, pp. 1–8, 2022.

[78] K. Baek, S. Shin, and H. So, "Decoupling thermal effects in GaN photodetectors for accurate measurement of ultraviolet intensity using deep neural network," *Engineering Applications of Artificial Intelligence*, vol. 123, Article ID 106309, 2023.

[79] M. Wang and W. Deng, "Deep visual domain adaptation: a survey," *Neurocomputing*, vol. 312, pp. 135–153, 2018.

[80] F. Zhuang, Z. Qi, K. Duan et al., "A comprehensive survey on transfer learning," *IEEE*, vol. 109, pp. 43–76, 2021.